

Synthesis, structure and anisotropy of thermoelectric properties of $\text{Bi}_2\text{Te}_{2.7}\text{Se}_{0.3}$ compound doped with samarium

© M.N. Yaprıntsev¹, O.N. Ivanov², A.E. Vasil'ev¹, M.V. Zhezhu¹, D.A. Popkov¹

¹ Shukhov State Technological University,
308012 Belgorod, Russia

² Belgorod National Research University,
308015 Belgorod, Russia

E-mail: yaprintsev@bsu.du.ru

Received August 12, 2021

Revised August 28, 2021

Accepted August 28, 2021

We study crystallographically textured thermoelectric materials with electronic conductivity based on bismuth telluride doped with samarium ($\text{Bi}_{2-x}\text{Sm}_x\text{Te}_{2.7}\text{Se}_{0.3}$, where $x = 0, 0.05, 0.02, 0.05$) obtained by the method of solvothermal synthesis and double pressing by the method of spark plasma sintering. The crystallographic texture was achieved by the spark plasma sintering of plate-like nanoparticles. The texturing axis [001] coincided with the direction of compression in the of spark plasma sintering process. An increase in the samarium concentration leads to a decrease in the radial size of the synthesized nanoplates, which facilitates the processes of rotation and sliding of particles relative to each other during pressing and, as a consequence, an increase in the anisotropy factor characterizing the degree of preferred grain orientation in the bulk material. Samarium doping affects the particle size of the initial powder, the average grain size in the bulk material and, as a consequence, the thermoelectric properties. It was found that the maximum of thermoelectric figure of merit weakly depends on the samarium content and falls in the range of $\sim (0.6-0.7)$, while the temperature position of the maxima noticeably shifts to higher temperatures with an increase in the Sm content.

Keywords: thermoelectric materials, bismuth telluride, spark plasma sintering, texturing, anisotropy in properties.

DOI: 10.21883/SC.2022.14.53856.16

The recovery of energy wasted in the form of heat in transport, industrial, and household processes is a task that is important and relevant in both economic and ecological terms [1,2]. In order to achieve this goal, one needs to construct a distributed network of modular and cost-efficient systems that convert heat into electricity. Solid-state thermoelectric devices used for small-scale and portable electrical generation are the most promising (and, in certain cases, are the sole option). Such devices may be of almost arbitrary size, are noted by their high strength and exceptional reliability, and may be adapted to energy collection from any heat source [1,3]. However, their economic efficiency needs to be enhanced prior to large-scale implementation. This may be done by increasing the efficiency of energy conversion and (or) reducing the production costs. The efficiency of energy conversion with thermoelectric devices is governed by thermoelectric figure of merit (Z) of the materials used. The dimensionless thermoelectric figure of merit is expressed as $ZT = S^2 \cdot T / \rho \cdot k$, where T is absolute temperature, ρ is the electric resistivity, S is the Seebeck coefficient, and k is the thermal conductivity [2,4–6]. Bismuth telluride Bi_2Te_3 and compounds based on it (both n -type and p -type) are currently considered to be the best thermoelectric materials for low-temperature applications. The high anisotropy of transport properties, such as the electric and thermal conductivity [7–13], is one of the specific features of bismuth telluride and

compounds based on it that has a significant effect on their thermoelectric properties. Bi_2Te_3 -based materials feature crystal structure anisotropy that is largely governed by the combination of various types of bonds between atoms [7]. The aim of the present study is to produce an n -type $\text{Bi}_{2-x}\text{Sm}_x\text{Te}_{2.7}\text{Se}_{0.3}$ thermoelectric with different concentrations of Sm ($x = 0, 0.005, 0.02, \text{ and } 0.05$) and reveal the specifics of Sm influence on the microstructural features and the anisotropy of thermoelectric properties.

Analytically pure chemical substances ($\text{Bi}(\text{NO}_3)_3 \cdot 5\text{H}_2\text{O}$, TeO_2 , SeO_2 , $\text{Sm}(\text{NO}_3)_3 \cdot 6\text{H}_2\text{O}$, NaOH , poly(1-ethenylpyrrolidin-2-one), and ethane-1,2-diol) were used to synthesize the initial powders. At the first stage of synthesis, $\text{Bi}(\text{NO}_3)_3 \cdot 5\text{H}_2\text{O}$, TeO_2 , SeO_2 , and $\text{Sm}(\text{NO}_3)_3 \cdot 6\text{H}_2\text{O}$ powders taken in the stoichiometric ratio were dissolved in a mixture of 600 cm³ of ethane-1,2-diol and 15 g of NaOH with vigorous stirring by a magnetic mixer. Poly(1-ethenylpyrrolidin-2-one) ($M_r = 12\,000$) was then added to the reaction mixture. After that, the system was heated to 185°C, held for 6 h, and cooled to room temperature. A dark gray residue was isolated by centrifugation and rinsed several times with anhydrous propan-2-ol. The obtained powder was dried at 60°C for 8 h. In order to prepare bulk samples, the powdered material was compacted by spark plasma sintering (SPS) under a pressure of 40 MPa for 2 min in vacuum at a

Elemental composition, average size of the initial particles, average grain size, anisotropy factor, and majority-carrier density for $\text{Bi}_{2-x}\text{Sm}_x\text{Te}_{2.7}\text{Se}_{0.3}$ samples with different concentrations of samarium

Concentration of Sm (x)	Element (at%)				d_{\perp} , nm	d_{\parallel} , nm	D_{\perp} , nm	D_{\parallel} , nm	F	N , cm^{-3}
	Bi	Sm	Te	Se						
0	39.95	–	54.11	5.94	523	55	797	111	12	$1.25 \cdot 10^{19}$
0.005	40.06	0.08	53.85	6.01	496	49	776	113	21	$2.98 \cdot 10^{19}$
0.02	39.55	0.42	54.12	5.91	461	52	718	115	29	$2.84 \cdot 10^{19}$
0.05	38.96	0.99	53.97	6.08	424	53	668	118	39	$2.91 \cdot 10^{19}$

temperature of 680 K. The prepared samples were ground up and compacted again in the same conditions.

The density of bulk $\text{Bi}_{2-x}\text{Sm}_x\text{Te}_{2.7}\text{Se}_{0.3}$ samples was measured using the Archimedean method. X-ray diffraction analysis was performed using a Rigaku Ultima IV diffractometer ($\text{CuK}\alpha$ radiation) to determine the crystal structure and the phase composition of the initial powders and bulk materials. A Nova NanoSEM 450 scanning electron microscope (SEM) was used to determine the morphology of the initial powders, estimate the particle size, and examine the specifics of the grain structure of bulk samples. A Shimadzu ICPE-9000 inductively coupled plasma optical emission spectrometer was used for quantitative elemental analysis of the obtained bulk samples. Rods $2 \times 2 \times 10$ mm in size and disks $\varnothing 10 \times 2$ mm were prepared for measurements of the thermoelectric properties; a total of two sets of samples cut in directions mutually perpendicular relative to the pressing axis were produced for each studied material. A ULVAC ZEM-3 measurement system was used to determine ρ and S . The value of k was measured using a ULVAC TC-1200 system.

A typical powder diffraction pattern for the initial $\text{Bi}_{2-x}\text{Sm}_x\text{Te}_{2.7}\text{Se}_{0.3}$ powder is presented in Fig. 1, *a*. All the obtained powders are single-phase with a rhombohedral crystal structure (space group of symmetry $R\bar{3}m$), which is typical of compounds based on bismuth telluride (PDF#01-089-4302). All powdered materials have similar morphologies of particles that may be characterized as hexagonal plates (Fig. 1, *c*). SEM images were analyzed to estimate the average diameter (D_a) and thickness (d_a) of particles in a powder and grains in a bulk material; the obtained data were then used to plot histograms of the particle size distribution. The average size of powder particles and grains is presented in the table. The formation of hexagonal plates is typical of Bi_2Te_3 -based compounds [7–13].

The results of quantitative elemental analysis (see the table) reveal that the chemical composition of the obtained samples is close to the target one. The density of all bulk samples was $\sim 7.5 \text{ g/cm}^3$, which amounts to $\sim 96\%$ of the theoretical density (7.8 g/cm^3 according to [14]). The results of X-ray diffraction analysis demonstrated that

all bulk samples have a well-pronounced crystallographic texture. The intensity of peaks (001) increased in the diffraction patterns from the surfaces of bulk samples oriented perpendicularly to the pressing direction (Fig. 1, *b*). This redistribution of peak intensities is attributable to the formation of a lamellar texture with preferred grain orientation in the direction perpendicular to the pressing direction. The texturing degree of $\text{Bi}_{2-x}\text{Sm}_x\text{Te}_{2.7}\text{Se}_{0.3}$ samples, which characterizes the degree of preferred grain orientation, was estimated using the Lotgering factor, F [15] (see the table).

It is evident that the texturing degree increases with x . The variation of the grain structure and the texturing degree with samarium concentration may be associated with the corresponding change in the degree of chemical bond polarity (electronegativity difference) [7]. Figures 1, *d* and *e* demonstrate the SEM images of grain structures on cleavage surfaces oriented perpendicularly (*d*) and parallel (*e*) to the pressing direction. A disordered grain structure with average grain size D_{\perp} and a predominantly irregular grain shape is seen in Fig. 1, *d*. In contrast, grains in Fig. 1, *e* form an ordered lamellar structure with average thickness D_{\parallel} (see the table). Lamellar sheets line in the plane perpendicular to the pressing direction. This grain ordering is induced by the processes of rotation and sliding of the initial plate-like particles in the course of uniaxial compression during spark plasma sintering. Thus, the SEM images in Fig. 1, *d* and *e* agree with the results of X-ray diffraction analysis.

Figure 2 presents the $\rho(T)$ dependences measured perpendicular and parallel to the pressing direction for samples with different samarium concentrations. The value of ρ increases with temperature for all measurement directions in all the studied samples. This is typical of metals or degenerate semiconductors and is associated with carrier scattering off phonons, which leads to a reduction in mobility. As x grows, ρ decreases. This trend is correlated with the anisotropy factor enhancement. Since the carrier density is almost the same in doped samples (see the table), the variation of carrier mobility should be regarded as a mechanism behind the ρ changes in the studied samples. The values of ρ measured in

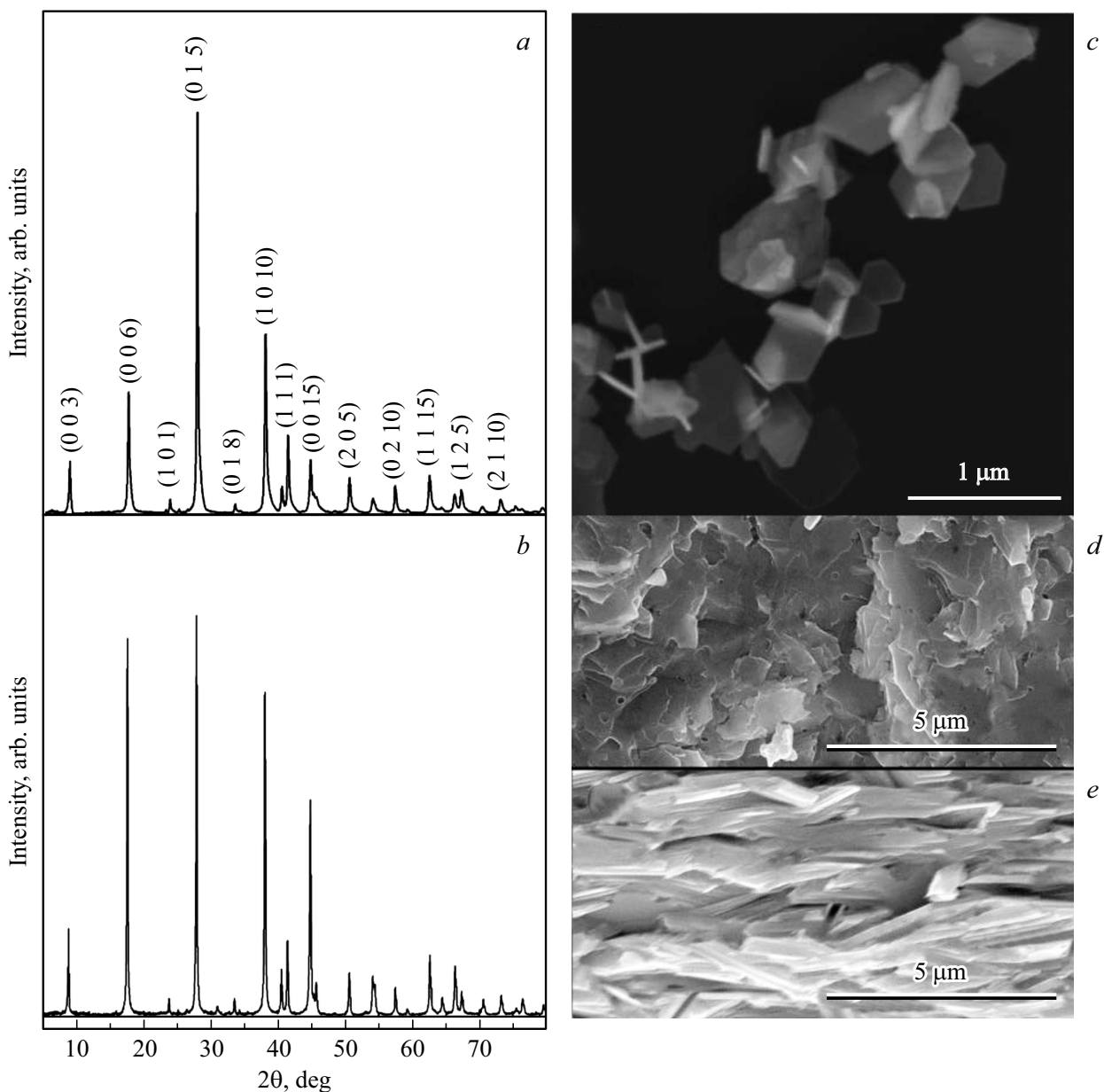


Figure 1. Diffraction patterns of the initial powder (*a*) and the bulk material (*b*) from the surface oriented perpendicularly to the pressing axis; SEM image of the initial powder (*c*); SEM images of cleavage surfaces oriented perpendicularly (*d*) and parallel (*e*) to the pressing direction for the $\text{Bi}_{1.95}\text{Sm}_{0.05}\text{Te}_{2.7}\text{Se}_{0.3}$ sample.

different directions for samples of the same composition differ.

The resistance measured perpendicular to the pressing axis is lower than the one measured in the parallel direction. This is attributable to the grain-size differences in these directions and the differences in carrier mobility due to scattering off grain boundaries. The Seebeck coefficient assumes negative values for all measurement directions in all the studied samples, which are *n*-type semiconductors (Fig. 3).

The value of S decreases as the samarium concentration increases. All the $S(T)$ curves feature a maximum

related to the bipolar effect [16–20], and this maximum shifts toward higher temperatures as x grows. The values of S measured in mutually perpendicular directions for samples of the same composition exhibit a well-pronounced anisotropy. The temperature dependences of the overall thermal conductivity of samples are presented in Fig. 4. The presence of minima in curves $k(T)$ is attributable to the alteration of thermal conductivity mechanisms (phonon, electron, and bipolar thermal conductivity [7–13,21]).

The room-temperature thermal conductivity values measured in the same direction for samples with different x

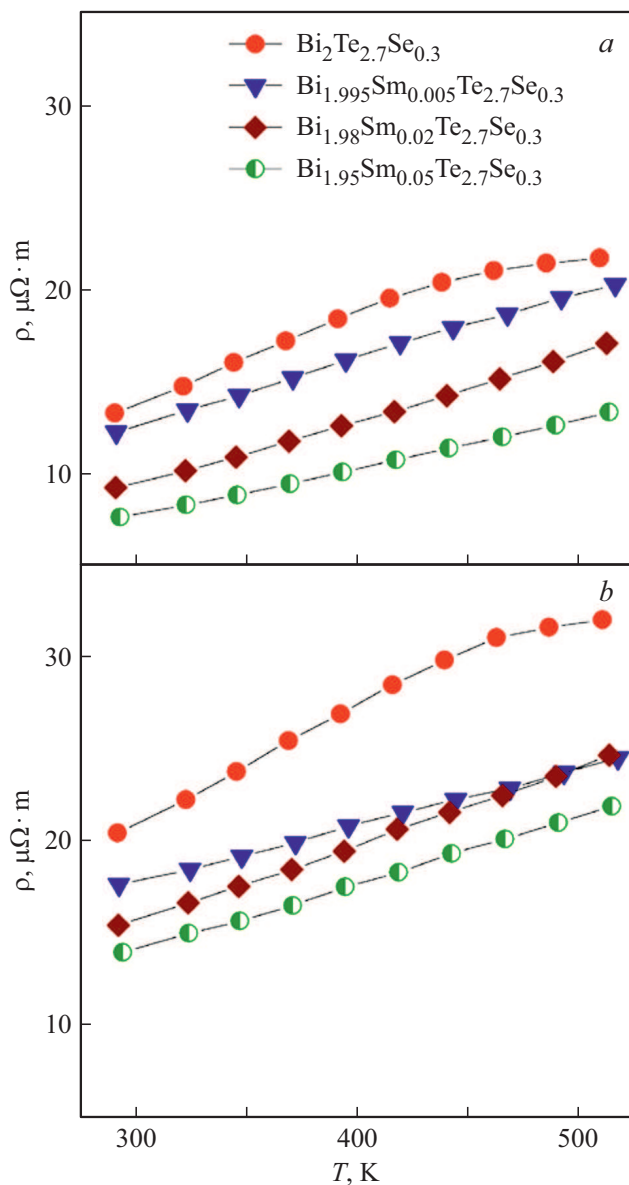


Figure 2. Temperature dependences of the electric conductivity measured in the direction perpendicular (a) and parallel (b) to the pressing axis for samples with different samarium concentrations.

are close. The presence of a crystallographic texture and grain-size anisotropy in directions mutually perpendicular relative to the pressing axis results in a strong k anisotropy. The thermal conductivity measured in the perpendicular direction is significantly higher than the one measured in the parallel direction. The values of ρ , S , and k measured in mutually perpendicular directions were used to plot the $ZT(T)$ dependences for samples with different x values (Fig. 5).

All these $ZT(T)$ dependences have maxima that shift toward higher temperatures as the samarium concentration grows. The presence of maxima may be attributed to the intrinsic conductivity at high temperatures. The

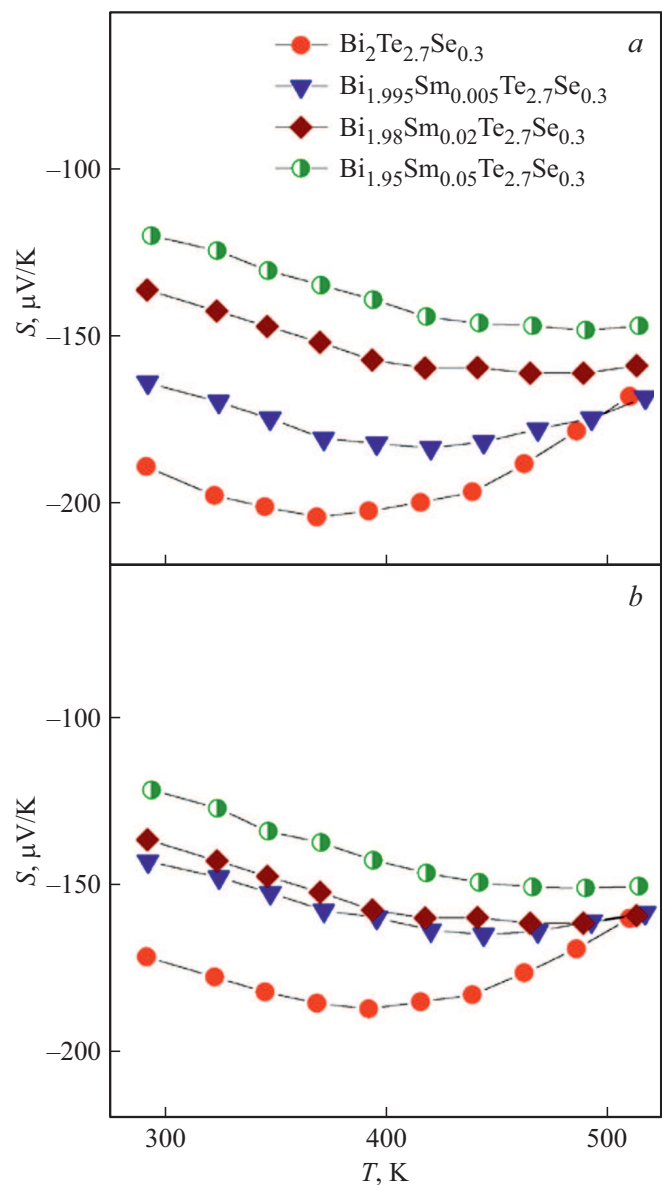


Figure 3. Temperature dependences of the Seebeck coefficient measured in the direction perpendicular (a) and parallel (b) to the pressing axis for samples with different samarium concentrations.

maximum ZT value depends only weakly on x and falls within the range of $\sim (0.6-0.7)$. Both the electric resistance and the Seebeck coefficient decrease after doping with Sm. Thus, this doping does not allow one to raise ZT . However, the ZT maximum shifts toward higher temperatures when x increases. This effect is important for thermoelectric applications, since it may alter the operating temperature range of thermoelectric devices.

Funding

This study was supported financially by the Russian Foundation for Basic Research as part of scientific project

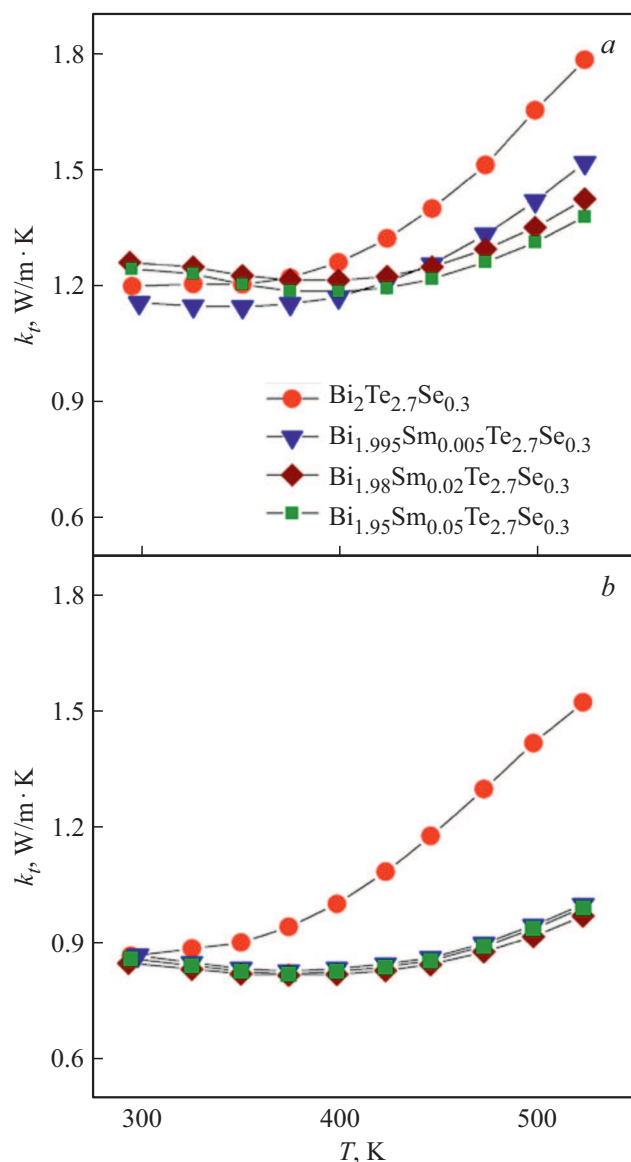


Figure 4. Temperature dependences of the thermal conductivity measured in the direction perpendicular (a) and parallel (b) to the pressing axis for samples with different samarium concentrations.

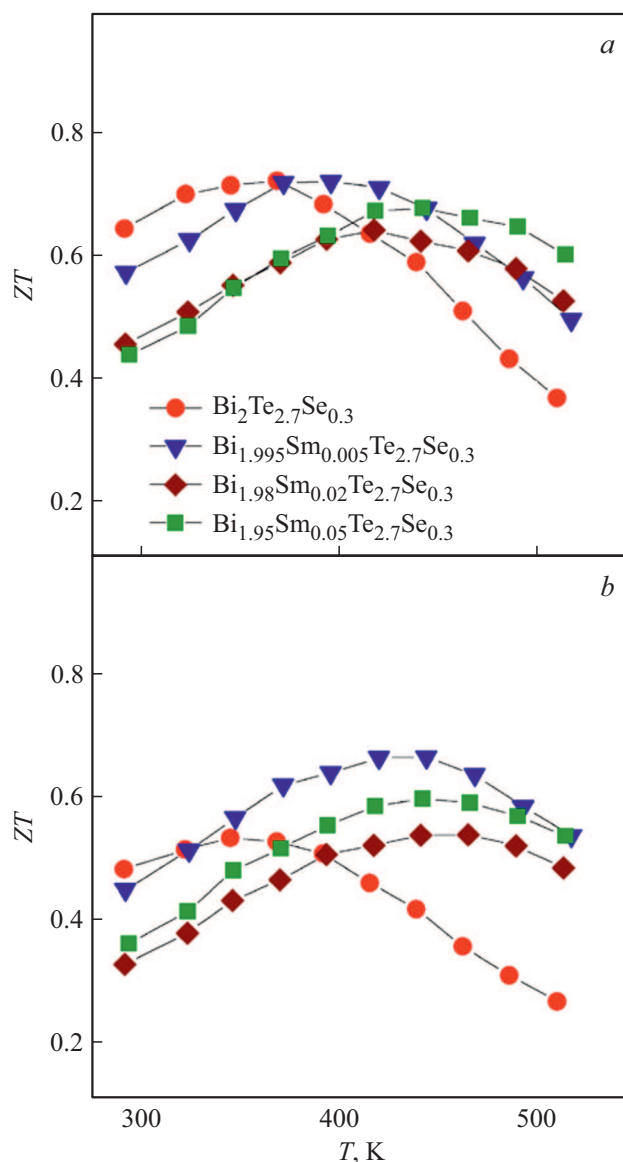


Figure 5. Temperature dependences of the thermoelectric figure of merit calculated in the direction perpendicular (a) and parallel (b) to the pressing axis for samples with different samarium concentrations.

No. 20-03-00672. All experiments were performed using the equipment provided by the „Technology and Materials“ common use center of the Belgorod State University.

Conflict of interest

The authors declare that they have no conflict of interest.

References

- [1] L.E. Bell. *Science*, **321**, 1457 (2008).
- [2] G.J. Snyder, E.S. Toberer. *Nature Mater.*, **7**, 105 (2008).
- [3] S.I. Kim, K.H. Lee, H.A. Mun, H.S. Kim, S.W. Hwang, J.W. Roh, D.J. Yang, W.H. Shin, X.S. Li, Y.H. Lee, G.J. Snyder, S.W. Kim. *Science*, **348**, 109 (2015).
- [4] S. Ortega, M. Ibañez, Y. Liu, Y. Zhang, M.V. Kovalenko, D. Cadavid, A. Cabot. *Chem. Soc. Rev.*, **46**, 3510 (2017).
- [5] M. Ibañez, Z. Luo, A. Genc, L. Piveteau, S. Ortega, D. Cadavid, O. Dobrozhan, Y. Liu, M. Nachttegaal, M. Zebarjadi, J. Arbiol, M.V. Kovalenko, A. Cabot. *Nature Commun.*, **7**, 10766 (2016).
- [6] R.J. Mehta, Y. Zhang, C. Karthik, B. Singh, R.W. Siegel, T. BorcaTasciuc, G.A. Ramanath. *Nature Materials*, **11**, 233 (2012).
- [7] Y. Liu, Y. Zhang, K.H. Lim, M. Ibañez, S. Ortega, M. Li, J. David, S.M. Sanchez, K.M. Ng, J. Arbiol, M.V. Kovalenko, D. Cadavid, A. Cabot. *ACS Nano*, **12** (7), 7174 (2018)

- [8] M. Yaprıntsev, O. Ivanov, A. Vasil'ev, M. Zhezhu, E. Yaprıntseva. *J. Solid State*, **297**, 122047 (2021)
- [9] O. Ivanov, M. Yaprıntsev, A. Vasil'ev. *J. Solid State*, **290**, 121559 (2020)
- [10] O. Ivanov, M. Yaprıntsev, A. Vasil'ev. *J. Eur. Ceramic Soci.*, **40**, 3431 (2020).
- [11] M. Yaprıntsev, A. Vasil'ev, O. Ivanov. *J. Eur. Ceramic Soc.*, **40**, 742 (2020)
- [12] M. Yaprıntsev, A. Vasil'ev, O. Ivanov. *J. Eur. Ceramic Soc.*, **39**, 1193 (2019)
- [13] A. Vasil'ev, M. Yaprıntsev, O. Ivanov, E. Danshina. *Solid State Sci.*, **84**, 28 (2018)
- [14] F. Wu, H.Z. Song, J.F. Jia, F. Gao, Y.J. Zhang, X. Hu. *Phys. Status Solidi*, **210**, 1183 (2013)
- [15] F.K. Lotgering. *J. Inorg. Nucl. Chem.*, **9**, 113 (1959).
- [16] D.C. Ghosh, R. Biswas. *Int. J. Mol. Sci.*, **3**, 87 (2002).
- [17] M.V. Putz, N. Russo, E. Sicilia. *J. Phys. Chem. A*, **107**, 5461 (2003).
- [18] N.T. Nghi, A.L. Usiikans, T.A. Cherepanova. *Cryst. Res. Technol.*, **21**, 367 (1986).
- [19] M. Yaprıntsev, R. Lyubushkin, O. Soklakova, O. Ivanov. *J. Electron. Mater.*, **47**, 1362 (2018).
- [20] Z. Sary, J. Horak, M. Stordeur, M. Stolzer. *J. Phys. Chem. Solids*, **49**, 29 (1988).
- [21] Q. Lognon, F. Gascoin, O.I. Lebedev, L. Lutterotti, S. Gascoin, D. Chateigner. *J. Am. Ceram. Soc.*, **97**, 2038 (2014).